RSC Advances

PAPER

View Article Online
View Journal | View Issue

Cite this: *RSC Adv.*, 2021, **11**, 24816

Terpyridine-derived perovskite single crystals with tunable structures and electronic dimensionality†

Yaxuan Yuan,[a] Yeming Xian,[a] Yi Long,[a] Yangyi Zhang,[a] Naveed Ur Rahman,[a] Yongli Zhang,*[b] Jiandong Fan[a] and Wenzhe Li *[a]

Received 21st May 2021
Accepted 3rd July 2021

DOI: 10.1039/d1ra03957a

rsc.li/rsc-advances

Dimensionality engineering has proved to be a reliable strategy for addressing the issue of perovskite stability. In this study, a series of previously unreported low-dimensional organic–inorganic hybrid perovskite single crystals were designed and grown by following a simple hydrothermal approach involving solution processing. The as-prepared terpyridine-derived perovskite single crystals displayed tunable structures and electronic dimensionality, which was closely associated with the crystal growth conditions. The performed DFT calculations suggested that the fluctuating conduction band edge demonstrates obvious charge delocalization associated with the π-conjugation effect, a feature promoting efficient charge transport by means of coupling structural dimensionality and electronic dimensionality. This study has provided new ideas for the design of new materials to be used in fields involving photovoltaic devices.

Hybrid organic–inorganic perovskites have attracted intense research interest as active materials for electronic and optoelectronic applications[1–5] because of their high absorption coefficients,[6,7] high carrier mobility levels[8,9] and tunable band gaps,[10–12] among other features. The development of organic–inorganic hybrid perovskite solar cells has proceeded rapidly, and such devices with energy conversion efficiency levels exceeding 25.5% have been produced in the past decade.[13–15] The widely-employed perovskite materials include $CH_3NH_3PbI_3$ ($MAPbI_3$) and $[HC(NH_2)_2]PbI_3$ ($FAPbI_3$), which are three-dimensional (3D) hybrid organic–inorganic hybrid perovskites.[6,16] Compared with the 3D organic–inorganic hybrid perovskites, low-dimensional (LD) perovskites have received considerable attention recently because of their structural versatility, *e.g.*, 2D materials with layer structures, 1D perovskites with connected octahedra and 0D materials with isolated octahedra.[17,18] It is noteworthy that a particularly diverse variety of 0D and 1D perovskites have been made by incorporating organic cations with different sizes inside the Pb–I framework as a result of being able to relax restrictions on the sizes of the cations.[19–22] The 1D and 1D–2D or 1D–3D halide perovskite materials have recently emerged as a highly promising class of functional materials for a variety of applications. It has been found that deposition of a 1D layer on top of a 3D material can increase the air and heat stabilities of the corresponding device,[23] and that formation of 0D–2D hybrids can simultaneously improve photoresponses and yield higher performance levels in optoelectronic devices.[24] These dimensionally hybrid perovskite materials could be a superior choice for acquiring stable perovskite solar cells. Concurrently, numerous methods involving manipulating the components and growth conditions have been developed to control these structures and hence enable the acquisition of unique structural characteristics of perovskites.[25–28] In this scenario, investigating and developing novel LD perovskites by carrying out molecular crystal engineering provides a new paradigm for constructing and developing new perovskites-based optoelectronic devices.

In this study, we innovatively mixed certain amounts of 2,2:6,2-terpyridine (Tpy, J&K, >98%) and PbI_2 as the precursors to grow a new class of perovskite single crystals by means of a hydrothermal method involving solution processing. The dimensions and structures of the as-prepared perovskite single crystals were controlled by tuning the growth pattern and introduced concentration of HI, which allowed for an acquisition of a series of 0D and 1D terpyridine-based perovskite single crystals. The structures of the new crystals were resolved and refined, and the corresponding energy band structure, state density and charge density distribution were obtained from density functional theory (DFT) calculations. The present work has provided a potential way to regulate the structure, namely by introducing organic cations into the perovskite structure and changing growth conditions, with this approach expected to allow for further improvements of the performances of perovskite-based photoelectronic devices in general.

[a]*Institute of New Energy Technology, Department of Electronic Engineering, College of Information Science and Technology, Jinan University, Guangzhou, 510632, China. E-mail: li_wz16@jnu.edu.cn*

[b]*Department of Ecology, College of Life Science and Technology, Jinan University, Guangzhou, 510632, China, . E-mail: zhangyl@jnu.edu.cn*

† Electronic supplementary information (ESI) available. CCDC 2081449–2081451. For ESI and crystallographic data in CIF or other electronic format see DOI: 10.1039/d1ra03957a

Tpy_2PbI_6 single crystal

Herein, we innovatively obtained the 0D Tpy_2PbI_6 perovskite structure. This material was grown by slowly cooling a saturated perovskite precursor solution containing stoichiometric amounts of Tpy and PbI_2; the cooling was achieved by following a gradient cooling procedure and was carried out from 180 °C to room temperature (Fig. 1). Fig. 1 shows the microstructure along the <0 0 1> crystallographic orientation. At high temperatures of up to 180 °C, with the components in the precursor solution vibrating violently, the 0D Tpy_2PbI_6 perovskite single crystal was obtained. The two building blocks in this case were the inorganic $[PbI_6]^{4-}$ octahedron and the organic cation $[Tpy]^{2+}$. The detailed bond lengths of Pb–I are shown in Fig. 2. One Pb atom was observed to be coordinated with six I atoms. In the case of Tpy_2PbI_6, its $[PbI_6]^{4-}$ octahedra were compressed, due to a Jahn–Teller distortion involving the two opposite Pb–I bonds being shorter than the other four Pb–I bonds, and this compression was deemed to be associated with the rigidity of the Tpy. Moreover, the organic components were identified to be conjugated along the <0 0 1> direction. This microstructure led to the monoclinic (C 1 2/m 1 space group) symmetry, and the lengths of its unit cell were measured to be $a = 13.0069(3)$ Å, $b = 14.6783(3)$ Å and $c = 10.1587(3)$ Å. The 0D Tpy_2PbI_6 perovskite single crystal was assumed to be structurally unstable, considering the island-like nature of the $[PbI_6]^{4-}$ octahedra in the perovskite lattice.

$Tpy_4Pb_5I_{18}$ single crystal

The 1D $Tpy_4Pb_5I_{18}$ was obtained at a relatively low temperature of 140 °C. Here, one Pb atom coordinated six I atoms, and the corresponding bond lengths were found to be diverse, ranging from 3.1258 to 3.3439 Å, and accordingly giving rise to a distorted $[PbI_6]^{4-}$ octahedron. The five $[PbI_6]^{4-}$ octahedra on each short chain of the 1D $Tpy_4Pb_5I_{18}$ single crystal exhibited a linear arrangement *via* sharing the I–I edge of the octahedron while each of the two parts was connected *via* sharing the I corner (Fig. 1). The Tpy group was observed to be arranged along both sides of the octahedra and they repeated along the <0 0 1> crystal direction. Significantly, only one N atom was observed to be bound to the H atom in the Tpy organic part of the 1D $Tpy_4Pb_5I_{18}$ single crystal, in contrast to two N atoms bound to the H atoms in the 0D structure. Overall, the linear metal halide chains were observed to be spaced apart by the TPy organic cations to form a bulk assembly of 1D halide perovskites with cell parameters of $a = 12.8492(2)$ Å, $b = 12.89296(18)$ Å and $c = 15.7151(2)$ Å.

$Tpy_2Pb_3I_6$ single crystal

Using a relatively low concentration of hydroiodic acid in the precursor solution, we obtained a 1D $Tpy_2Pb_3I_6$ single crystal. Here the $[PbI_6]^{4-}$ octahedra and $[PbN_3I_2]^{3-}$ octahedra arranged themselves in an alternating fashion *via* sharing the I–I edge of the octahedron, and the Pb–Tpy complexes alternated between the two sides of the octahedron (Fig. 1). The Pb–I bond was found to be broken and a Pb–N bond formed during the crystallization, attributed to the different abilities of I and N to coordinate Pb. Thus, $Tpy_2Pb_3I_6$ crystallized in the orthorhombic *Pbcn* space group with cell parameters of $a = 22.4598(5)$ Å, $b = 14.6783(3)$ Å and $c = 10.1587(3)$ Å. More details of the data for the crystal diffraction refinements are summarized in Fig. S1.†

The measured powder X-ray diffraction (PXRD) pattern together with the calculated single-crystal X-ray diffraction (SCXRD) pattern confirmed the high purity of the crystals

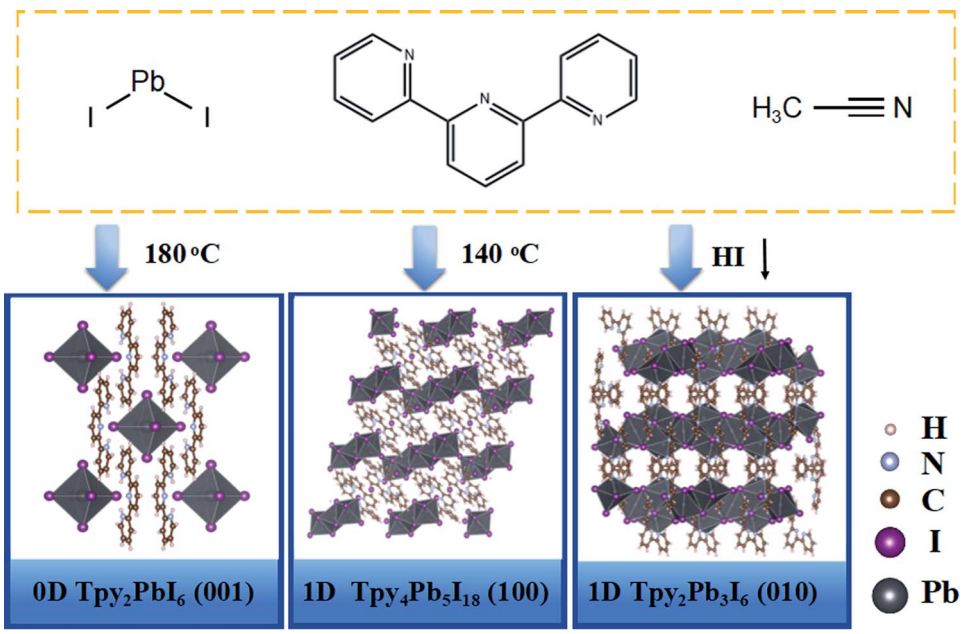

Fig. 1 Structures of 0D Tpy_2PbI_6, 1D $Tpy_4Pb_5I_{18}$ and 1D $Tpy_2Pb_3I_6$ single crystals.

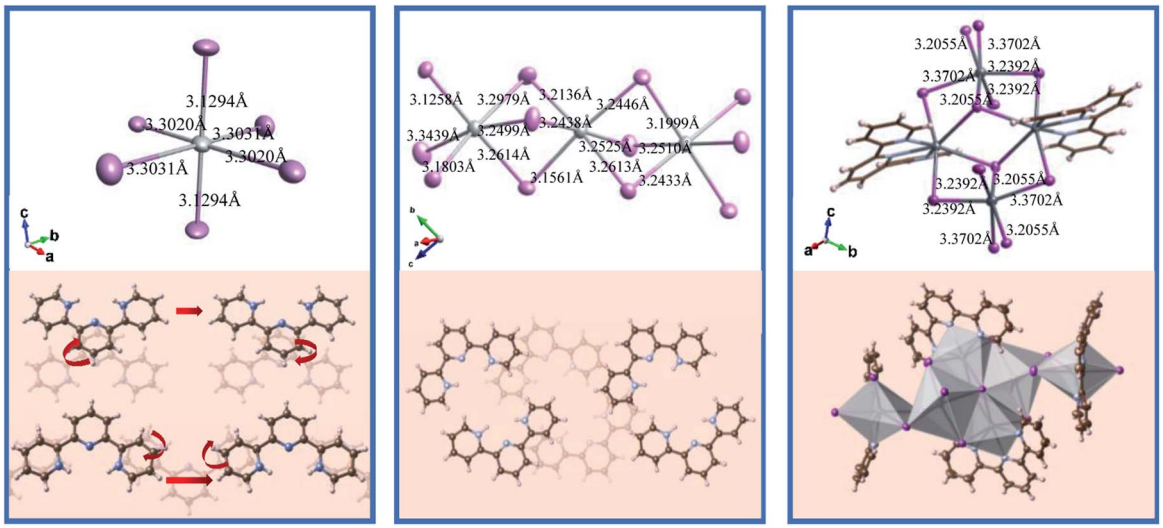

Fig. 2 Bond lengths and arrangements of $[PbI_6]^{4-}$ and $[PbN_3I_2]^{3-}$ in the as-prepared perovskite single crystals.

(Fig. S1†). The diffraction peaks were observed to be mainly at low angles for all of the cases, which were related to the low-dimensional octahedra. We took X-ray photoelectron spectroscopy (XPS) measurements to determine the elemental composition and valence states of the 0D Tpy_2PbI_6, 1D $Tpy_4Pb_5I_{18}$ and 1D $Tpy_2Pb_3I_6$ single crystals. As expected, the Pb 4f, I 3d, C 1s and N 1s peaks were evidently detected in the full spectrum scan, and the corresponding peaks at high resolution are also provided in Fig. S2.† The spectrum of the LD perovskite exhibited the characteristic I 4d peaks at 618.4–618.7 eV and 629.9–630.2 eV, with the observable differences in binding energies attributed to slightly different chemical environments of the Pb–I covalent bonds. Notably, the XPS results of all of the single crystals each showed a weak N 1s signal at about 400 eV, which could be split into two independent peaks as a consequence of the presence of two types of N in different chemical environments. The presence of the N 1s peak in the high-resolution spectrum of every sample suggested that the N signal derived from three components (Fig. 3). The main component at 399.2 eV can be reasonably attributed to the pyridine nitrogen.[29] The protonation of the nitrogen atom was related to these aromatic molecules acting as Lewis bases due to the free electron pairs of nitrogen atoms in the rings.[30] The other two components, located at higher binding energy levels (401.2 eV, 401.7 eV), were likely associated with the Tpy nitrogen atoms protonated in two different ways, in which the N atom coordinated with H atoms or the Pb atom in our system, respectively. Similarly, Pb 4f peaks for the $Tpy_2Pb_3I_6$ species were observed at positions corresponding to two different chemical environments, in agreement with the values reported for the single crystals of PbI_2-BPy(I) and PbI_2-BPy(II).[23] These results also demonstrated the simultaneous occurrence of two situations for $Tpy_2Pb_3I_6$: one having the Pb atom coordinated with both four I atoms and two N atoms, and the other having the Pb atom coordinated with six I atoms.

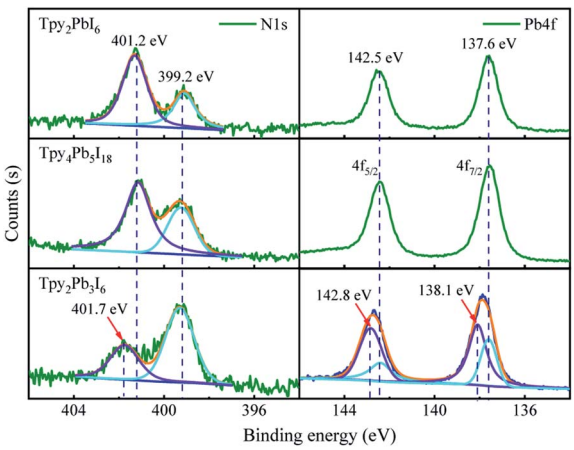

Fig. 3 N 1s and Pb 4f regions of the XPS spectra of Tpy_2PbI_6, $Tpy_4Pb_5I_{18}$ and $Tpy_2Pb_3I_6$ perovskite single crystals.

Fig. S3† shows the UV-Vis absorption spectra of the single crystals. The band edge exhibited a blue shift with the performed changes in temperature and content of HI in the precursor solution, and this shift was presumably associated with the structural arrangement between the organic cations and inorganic framework.[31] The strong absorption in the visible-light range indicated that these crystals may have potential applications in the field of photodetectors. The thermal stability of the as-prepared single crystals was investigated by conducting TGA/DSC characterizations from room temperature to 800 °C as shown in Fig. S4.† The results indicated decomposition temperatures of 220.0 °C, 225 °C and 274.06 °C for the as-prepared 0D Tpy_2PbI_6, 1D $Tpy_4Pb_5I_{18}$ and 1D $Tpy_2Pb_3I_6$ perovskites, respectively. The van der Waals and Coulomb forces in the low-dimensional structure were presumably too weak to resist the thermal vibrations of atoms.[23]

Fig. 4 shows the calculated band structure and projected density of states (PDOS) of the 0D Tpy_2PbI_6, 1D $Tpy_4Pb_5I_{18}$, and 1D $Tpy_2Pb_3I_6$ single crystals. The bandgaps were calculated to

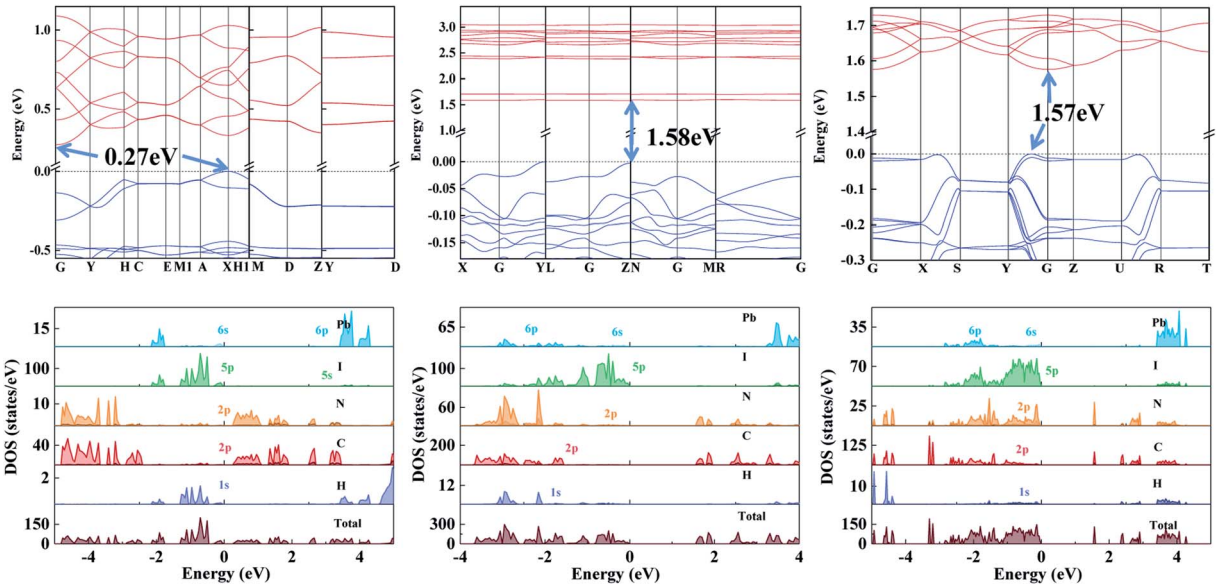

Fig. 4 The calculated band structure and projected density of states (PDOS) of the 0D Tpy_2PbI_6, 1D $Tpy_4Pb_5I_{18}$ and 1D $Tpy_2Pb_3I_6$ structures.

be 0.27 eV, 1.58 eV and 1.57 eV, respectively. For the 0D Tpy_2PbI_6 perovskite, the fluctuating conduction band edge indicated an obvious charge delocalization effect—with this effect originating from the π-conjugation effect, which enabled efficient charge transport through the Tpy as C-2p and N-2p orbital states in general make large contribution to such energy regions.[32,33] Note that the conjugation effect and corresponding electron delocalization on Tpy would promote charge transport as a result of strong orbital coupling.[33,34] In contrast, the relatively narrow energy band structure below the Fermi level was related to weak electron transfer between the isolated $[PbI_6]^{4-}$ octahedra in the inorganic framework. The interaction between the Pb–I octahedra was apparently strengthened when the temperature was decreased to 140 °C, leading to the formation of the crystal of 1D $Tpy_4Pb_5I_{18}$ with a direct bandgap. In the band diagram, within the range 1.5–2.0 eV, flat energy bands were observed and indicated a large electron effective mass; and the fluctuation of the energy band edge below the Fermi level further demonstrated relatively strong charge transport through the 1D Pb–I inorganic chains. In particular, the potential wells were distributed between the 1D Pb–I chains, which can be overcome by quantum tunneling, allowing subsequent charge transfer between Pb–I chains to occur. Fig. S5† shows the conduction band minimum (CBM)- and valence band minimum (VBM)-associated charge density distributions of the single crystals. The CBM-associated charges were indicated to be densely distributed throughout the $[PbI_6]^{4-}$ and $[PbN_3I_2]^{3-}$ complexes and the VBM-associated charges were indicated to be distributed on inorganic octahedral frameworks. The charge carrier transport would therefore be promoted through electronic dimensionality coupling in this scenario.

We compiled a table of single-crystal parameters and bandgap information on a series of organic–inorganic hybrid perovskite materials (Table 1). In comparison, the bandgaps of 0D Tpy_2PbI_6, 1D $Tpy_4Pb_5I_{18}$ and 1D $Tpy_2Pb_3I_6$ single crystals were found to be very similar to those of the previously reported hybrid perovskite materials,[23] and hence indicated the potential ability to use these materials as new alternative candidates for applications in solar cells and relevant photoelectric devices.

We calculated the trap-state density (N_{trap}) by means of characterizing the dark I–V curves of the perovskite single crystals. The applied voltage at the kink point is known as the trap-filled limit voltage (V_{TFL}), which allows for determining the trap density by using the equation $N_{trap} = V_{TFL}(2\varepsilon\varepsilon_0)/eL^2$, where L is the film thickness, and ε and ε_0 represent the elementary charge and vacuum permittivity, respectively.[35] As shown in Fig. S6,† the V_{TFL} values of Tpy_2PbI_6, $Tpy_4Pb_5I_{18}$ and $Tpy_2Pb_3I_6$ single crystals were determined to be 16.26, 21.71 and 24.17 V, respectively. The corresponding trap densities were determined from fittings and calculations to be 3.37×10^{11}, 4.51×10^{9} and 1.25×10^{11} cm^{-3}, respectively. Moreover, carrier mobility values were obtained using the equation $\mu = 8L^3J/9\varepsilon\varepsilon_0V^2$, where V is the applied voltage and J is the dark current;[37] the corresponding values were found to be 4.02×10^{-3}, 1.58×10^{-3} and 8.75×10^{-6} $cm^2\ V^{-1}\ S^{-1}$, respectively.

The VBM and CBM values of the three materials were obtained by means of the ultraviolet photoelectron spectrum (UPS) measurement. By calculating the energy levels of highest occupied molecular orbital (HOMO) and lowest unoccupied molecular orbital (LUMO), along with the optical band gap from the UV-vis result, we calculated the band gap alignment of single crystals shown in Fig. S8.† The VBM of 1D $Tpy_4Pb_5I_{18}$ and of 1D $Tpy_2Pb_3I_6$ was 5.40 eV, a value very similar to that of the widely used $MAPbI_3$ perovskite.

Conclusions

In summary, we grew a series of new terpyridine-derived perovskite single crystals, namely 0D Tpy_2PbI_6, 1D $Tpy_4Pb_5I_{18}$

Table 1 Details of X-ray crystallographic parameters and bandgaps of the as-prepared perovskite single crystals and some hybrid materials

Crystal type	PbI_2-PZPY[36]	$PbBr_2$-PZPY[36]	FAI-PbI_2-PZPY[36]	BPy-PbI_2(I)[23]	BPy-PbI_2(II)[23]	Tpy_2PbI_6[a]	$Tpy_4Pb_5I_{18}$[a]	$Tpy_2Pb_3I_6$[a]
Bandgap	—	—	—	2.23 eV	2.31 eV	1.61 eV	1.80 eV	1.76 eV
Crystal system	Triclinic	Triclinic	Triclinic	Monoclinic	Orthorhombic	Monoclinic	Triclinic	Orthorhombic
Space group	$P\bar{1}$	$P\bar{1}$	$P\bar{1}$	$C2/c$	$Fdd2$	$C\ 1\ 2/m1$	$P\bar{1}$	$Pbcn$
a (Å)	8.5138(7)	8.2505(5)	7.9331(6)	16.2729(3)	17.819(4)	13.0069(3)	12.8492(2)	22.4598(5)
b (Å)	10.0955(9)	9.4894(8)	12.2260(9)	10.3728(2)	4.5086(8)	14.6783(3)	12.89296(18)	12.1864(2)
c (Å)	15.8532(19)	14.9557(12)	9.5502(7)	8.2173(2)	11.1629(19)	10.1587(3)	15.7151(2)	14.0663(7)
α	83.390° (9)	83.981° (7)	90°	90°	90°	90°	86.4469° (11)	68.794° (4)
β	76.186° (9)	87.587° (6)	99.696° (8)	102.126° (2)	90°	107.854° (3)	70.5166° (13)	88.218° (3)
γ	89.800° (7)	88.916° (6)	90°	90°	90°	90°	72.3962° (13)	80.041° (3)

[a] As-prepared 0D Tpy_2PbI_6, 1D $Tpy_4Pb_5I_{18}$ and 1D $Tpy_2Pb_3I_6$ perovskite single crystals described in this paper.

and 1D $Tpy_2Pb_3I_6$, with controllable structures and electronic dimensionality by using a hydrothermal method involving solution processing. The conjugated structure and dimensionality transition associated with the organic part and the inorganic octahedral framework were carefully investigated. In particular, we were able to finely tune their structures and electronic dimensionality as well as their bandgaps by means of component and solvent engineering, capabilities beneficial for the subsequent control of the bandgap and carrier mobility levels of LD perovskites to be potentially used for applications in optoelectronic devices. We believe that the present study not only represents a step forward toward an in-depth understanding of the microstructures of perovskite single crystals, but also provides new avenues for investigating the incorporation of functionalized cations into the perovskite structures and designing novel solar cells and other perovskite-based photoelectronic devices.

Conflicts of interest

There are no conflicts to declare.

Acknowledgements

The research was funded by the Guangdong Basic and Applied Basic Research Foundation for Distinguished Young Scholar (No. 2019B151502030), National Natural Science Foundation of China (No. 22075103, 51872126, 51802120), Fundamental Research Funds for the Central Universities (No. 21621112), the Science and Technology Plan Project of Guangzhou (No. 202002030159) and Guangdong Basic and Applied Basic Research Foundation for Young Scholar (No. 2020A1515111057).

Notes and references

1 Z. Cheng and J. Lin, *CrystEngComm*, 2010, **12**, 2646–2662.
2 M. A. Green, A. Ho-Baillie and H. J. Snaith, *Nat. Photonics*, 2014, **8**, 506–514.
3 Y. N. Lu, J. X. Zhong, Y. Yu, X. Chen, C. Y. Yao, C. Zhang, M. Yang, W. Feng, Y. Jiang, Y. Tan, L. Gong, X. Wei, Y. Zhou, L. Wang and W. Wu, *Energy Environ. Sci.*, 2021, DOI: 10.1039/d1ee00918d.
4 W. Q. Wu, J. F. Liao, J. X. Zhong, Y. F. Xu, L. Wang and J. Huang, *Angew. Chem., Int. Ed. Engl.*, 2020, **59**, 20980–20987.
5 J. X. Zhong, W. Q. Wu, L. Ding and D. B. Kuang, *Energy Environ. Mater.*, 2020, 1–8.
6 W. Geng, L. Zhang, Y.-N. Zhang, W.-M. Lau and L.-M. Liu, *J. Phys. Chem. C*, 2014, **118**, 19565–19571.
7 A. Kojima, K. Teshima, Y. Shirai and T. Miyasaka, *J. Am. Chem. Soc.*, 2009, **131**, 6050–6051.
8 M. B. Johnston and L. M. Herz, *Acc. Chem. Res.*, 2016, **49**, 146–154.
9 C. Motta, F. El-Mellouhi and S. Sanvito, *Sci. Rep.*, 2015, **5**, 12746.
10 A. Amat, E. Mosconi, E. Ronca, C. Quarti, P. Umari, M. K. Nazeeruddin, M. Gratzel and F. De Angelis, *Nano Lett.*, 2014, **14**, 3608–3616.
11 S. A. Kulkarni, T. Baikie, P. P. Boix, N. Yantara, N. Mathews and S. Mhaisalkar, *J. Mater. Chem. A*, 2014, **2**, 9221–9225.
12 N. K. Kumawat, A. Dey, A. Kumar, S. P. Gopinathan, K. Narasimhan and D. Kabra, *ACS Appl. Mater. Interfaces*, 2015, **7**, 13119–13124.
13 M. A. Green, Y. Hishikawa, E. D. Dunlop, D. H. Levi, J. Hohl-Ebinger and A. W. Ho-Baillie, *Prog. Photovoltaics*, 2018, **26**, 427–436.
14 N. K. Tailor, M. Abdi-Jalebi, V. Gupta, H. Hu, M. I. Dar, G. Li and S. Satapathi, *J. Mater. Chem. A*, 2020, **8**, 21356–21386.
15 K. G. Lim, S. G. Ji, J. Y. Kim and T. W. Lee, *Small Methods*, 2020, **4**, 2000065.
16 C. C. Stoumpos, C. D. Malliakas and M. G. Kanatzidis, *Inorg. Chem.*, 2013, **52**, 9019–9038.
17 C. Lermer, S. T. Birkhold, I. L. Moudrakovski, P. Mayer, L. M. Schoop, L. Schmidt-Mende and B. V. Lotsch, *Chem. Mater.*, 2016, **28**, 6560–6566.
18 Z. Yuan, C. Zhou, Y. Tian, Y. Shu, J. Messier, J. C. Wang, L. J. van de Burgt, K. Kountouriotis, Y. Xin, E. Holt, K. Schanze, R. Clark, T. Siegrist and B. Ma, *Nat. Commun.*, 2017, **8**, 14051.
19 Y. Bekenstein, B. A. Koscher, S. W. Eaton, P. Yang and A. P. Alivisatos, *J. Am. Chem. Soc.*, 2015, **137**, 16008–16011.
20 C. L. C. Ellis, H. Javaid, E. C. Smith and D. Venkataraman, *Inorg. Chem.*, 2020, **59**, 12176–12186.

21 G. E. Eperon, S. D. Stranks, C. Menelaou, M. B. Johnston, L. M. Herz and H. J. Snaith, *Energy Environ. Sci.*, 2014, **7**, 982–988.
22 P. Srivastava, R. Kumar and M. Bag, *J. Phys. Chem. C*, 2020, **125**, 211–222.
23 P. Liu, Y. Xian, W. Yuan, Y. Long, K. Liu, N. U. Rahman, W. Li and J. Fan, *Adv. Energy Mater.*, 2020, **10**, 1903654.
24 J. S. Chen, T. L. Doane, M. Li, H. Zang, M. M. Maye and M. Cotlet, *Part. Part. Syst. Charact.*, 2017, **35**, 1700310.
25 M. H. Tremblay, A. M. Zeidell, S. Rigin, C. Tyznik, J. Bacsa, Y. Zhang, K. Al Kurdi, O. D. Jurchescu, T. V. Timofeeva, S. Barlow and S. R. Marder, *Inorg. Chem.*, 2020, **59**, 8070–8080.
26 G. García-Espejo, D. Rodríguez-Padrón, M. Pérez-Morales, R. Luque, G. de Miguel and L. Camacho, *J. Mater. Chem. C*, 2018, **6**, 7677–7682.
27 N. Marchal, W. Van Gompel, M. C. Gélvez-Rueda, K. Vandewal, K. Van Hecke, H.-G. Boyen, B. Conings, R. Herckens, S. Maheshwari, L. Lutsen, C. Quarti, F. C. Grozema, D. Vanderzande and D. Beljonne, *Chem. Mater.*, 2019, **31**, 6880–6888.
28 D. B. Mitzi, *J. Chem. Soc., Dalton Trans.*, 2001, 1–12.
29 M. Barber, J. Connor, M. Guest, I. Hillier, M. Schwarz and M. Stacey, *J. Chem. Soc., Faraday Trans. 2*, 1973, **69**, 551–558.
30 A. Yeşildağ and D. Ekinci, *Electrochim. Acta*, 2010, **55**, 7000–7009.
31 B. Chaudhary, T. M. Koh, B. Febriansyah, A. Bruno, N. Mathews, S. G. Mhaisalkar and C. Soci, *Sci. Rep.*, 2020, **10**, 1–11.
32 Y. Umemoto, Y. Ie, A. Saeki, S. Seki, S. Tagawa and Y. Aso, *Org. Lett.*, 2008, **10**, 1095–1098.
33 Y. Lin, L. Shen, J. Dai, Y. Deng, Y. Wu, Y. Bai, X. Zheng, J. Wang, Y. Fang, H. Wei, W. Ma, X. C. Zeng, X. Zhan and J. Huang, *Adv. Mater.*, 2017, **29**, 1604545.
34 Y. Zhang, Y. Duan, L. Song, D. Zheng, M. Zhang and G. Zhao, *J. Chem. Phys.*, 2017, **147**, 114905.
35 M. A. Lampert and P. Mark, *Current injection in solids*, Academic press, 1970.
36 J. Fan, Y. Ma, C. Zhang, C. Liu, W. Li, R. E. I. Schropp and Y. Mai, *Adv. Energy Mater.*, 2018, **8**, 1703421.
37 Q. Dong, Y. Fang, Y. Shao, P. Mulligan, J. Qiu, L. Cao and J. Huang, *Science*, 2015, **347**, 967–970.